$$E = \sum_{i=1}^{N} d_i^2 \tag{1}$$

The distance d_i is given by

$$d_i = \pm |\mathbf{q}_i - \mathbf{s}_i| \tag{2}$$

where $0 \le i < N$ and N is the number of contour points. Negative values indicate rays that cross the model surface.

The 3D pose of the femoral and tibial component model is estimated by minimizing the cost function E (equation (1)) iteratively using a nonlinear optimization technique [8]. A good function for determining convergence of the 3D pose of the model is given by root mean square distance (RMSD):

$$\mathrm{RMSD} = \sqrt{\sum_{i=0}^{N} d_i^2 \Big/ N} \tag{3}$$

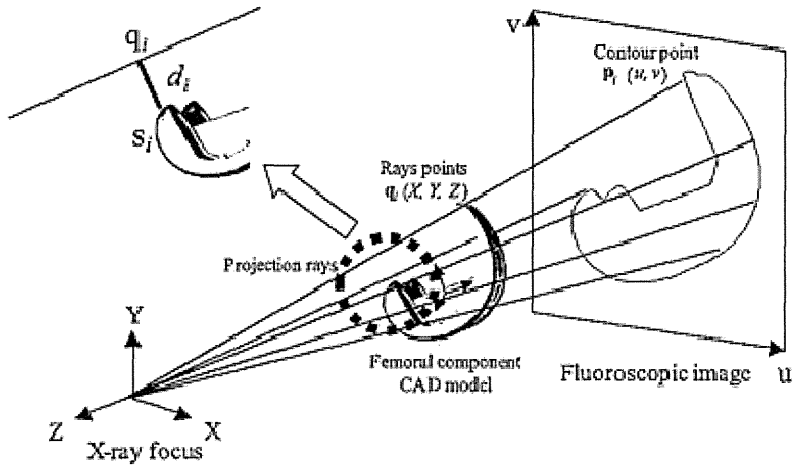

Figure 2. 3D pose estimation of the femoral component model from X-ray fluoroscopic images.

2.3 Pose estimation of mobile-bearing insert

To achieve 3D pose estimation of the mobile-bearing insert in TKA using X-ray fluoroscopy, tantalum beads are utilized. Because the polyethylene insert is transparent during fluoroscopy, four identical metallic tantalum beads are inserted at known positions of polyethylene insert using a specially designed insertion device during surgery. Holes of 2mm depth and small diameter are drilled, so that the 1 mm tantalum beads are press fitted in the predefined non-critical areas of the insert. Therefore, CAD model of the polyethylene insert can be created with the four strategically placed beads (Figure 3). Because three points are required on a rigid body to define its 3D pose, at least three beads have to be located on fluoroscopic images. Hence, all metallic beads were offset as far as possible from adjacent beads in the sagittal and frontal planes of the polyethylene insert, insuring optimal determination of out-of-plane rotations. Figure 4 shows a representative beads silhouette on the X-ray fluoroscopic image.

To extract these beads silhouette markers from the X-ray image, a Gaussian Laplacian filter and Canny's edge detector were applied [9], and false edges including implants contours and noises detected were manually erased. After the identification of the beads on each fluoroscopic image in this way, the 3D pose of the insert model is estimated using a feature-based 2D/3D registration technique, which uses beads silhouette on fluoroscopic image and the corresponding insert CAD model with beads. A cost function is defined as described above equation (1), and likewise 3D pose estimation of the mobile-bearing insert is performed.

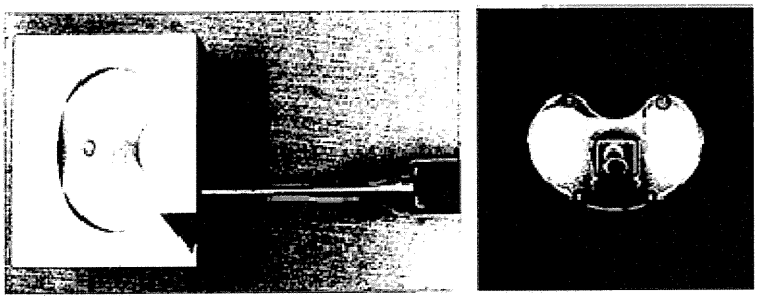

Figure 3. A specially designed insertion device (Left) and CAD model of the polyethylene insert with the four strategically placed beads (Right).

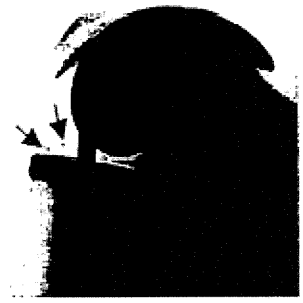

Figure 4. A representative beads X-ray image.

3. EXPERIMENTAL RUSULTS

3.1 Accuracy validation

In order to validate the accuracy of pose estimation for the mobile-bearing insert, two experiments were performed. In the first experiment, as a preliminary experiment, the repeatability of tantalum beads positions of polyethylene insert using a specially designed insertion device was investigated. Beads insertion of polyethylene insert using this device was repeated five times, beads positions of the five polyethylene inserts were accurately measured using high-resolution computed tomography. As a result of preliminary experiment, positional error of tantalum beads using this device was found to be 0.5 mm at most.

In the next experiment, based on the result of preliminary experiment, computer simulation test was performed. The positional errors within 0.5mm were randomly given for three or four strategically placed beads, and then synthetic tantalum beads silhouette images which had three or four beads were created for the insert in known typical orientations. In this study, a set of six synthetic tantalum beads silhouette images as shown in Figure 5 were used. The pose estimation errors of the insert were determined by comparing the estimated pose to the known pose.

The results of computer simulation test of pose estimation for the mobile-bearing insert are presented in Table 1. The root-mean-square errors (RMS errors) are given for each synthetic silhouette image. The RMS errors of all variables depended on the orientation pattern of the insert, while the difference of the error by beads projection number (three or four beads) for each orientation pattern (image 1,2 and image 3,4 and image 5,6) was small. The RMS errors of the five variables except for z (medial-lateral) translation were sufficiently smaller than 1.0 mm and 1.0 degree.

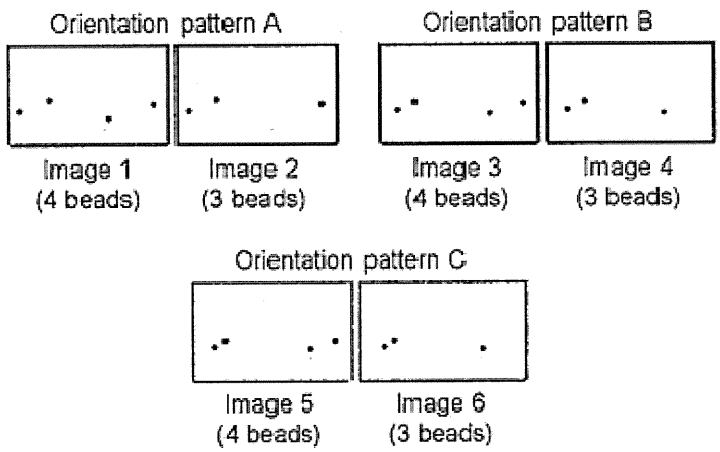

Figure 5. Synthetic tantalum beads silhouette images in typical orientations used for computer simulation test.

Table 1. Pose estimation errors for computer simulation test of the mobile-bearing insert.

RMS errors		Translation (mm)			Rotation (degrees)		
		x posterior-anterior	*y proximal-distal*	*z medial-lateral*	*x adduction-abduction*	*y internal-esternal*	*z extension-flexion*
Orientation pattern A	Image 1	0.20	0.17	0.83	0.13	0.27	0.22
	Image 2	0.30	0.48	0.99	0.14	0.30	0.22
Orientation pattern B	Image 3	0.43	0.14	0.96	0.18	0.47	0.32
	Image 4	0.41	0.39	1.02	0.23	0.43	0.34
Orientation pattern C	Image 5	0.52	0.67	1.48	0.49	0.53	0.47
	Image 6	0.65	0.84	1.63	0.51	0.58	0.45

3.2 Clinical applications

We finally applied the present technique to the mobile-bearing TKA patients during dynamic motion. The object of the study was explained to patients, and formal consent was obtained. Under fluoroscopic surveillance, dynamic movement in deep knee bending was conducted for total seven patients. Measurement values of each dynamic movement were described as the relative pose values of the femoral component with respect to the tibial component, and as that of the mobile-bearing insert with respect to the tibial component. For *in vivo* kinematic analysis, the relative pose of each knee implants model is determined by employing a three-axis Euler-angle system [10], and then the pose can be denoted by six variables, three translations and three rotations.

In the results of clinical applications, a representative image of the femoral and tibial CAD models overlaid on the X-ray image after 3D pose estimation, and an image of the mobile bearing insert estimated based on the metallic tantalum beads are shown in Figure 6. The sequence of relative poses in dynamic movement showed a smooth and reasonable physiologic pattern of motion, and the average range of motion for flexion-extension angle during the deep knee bending was 121.4 degree. In all seven patients, the femoral component rotated externally with respect to the tibial component during flexion, and the average external rotation range was 13.0 degree (Figure 7). Similarly, in all cases, the mobile-bearing insert also rotated externally with respect to the tibial component during flexion, and the average rotation range was 12.1 degree (Figure 8). In a few cases, the femoral component showed more external rotation than the mobile-bearing insert with respect to the tibial component during flexion, and the rotation angle was found to be about 5.0 degree at a maximum.

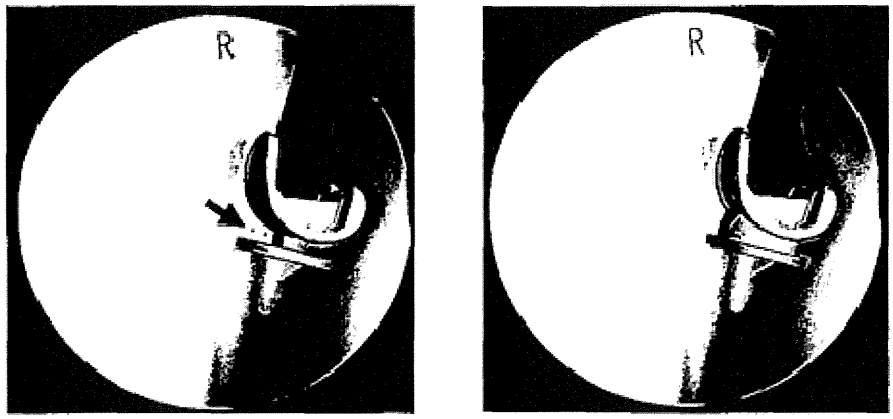

Figure 6. CAD model images from a representative TKA patient during deep knee bending. Femoral and tibial component models (Left) and mobile-bearing insert model (Right).

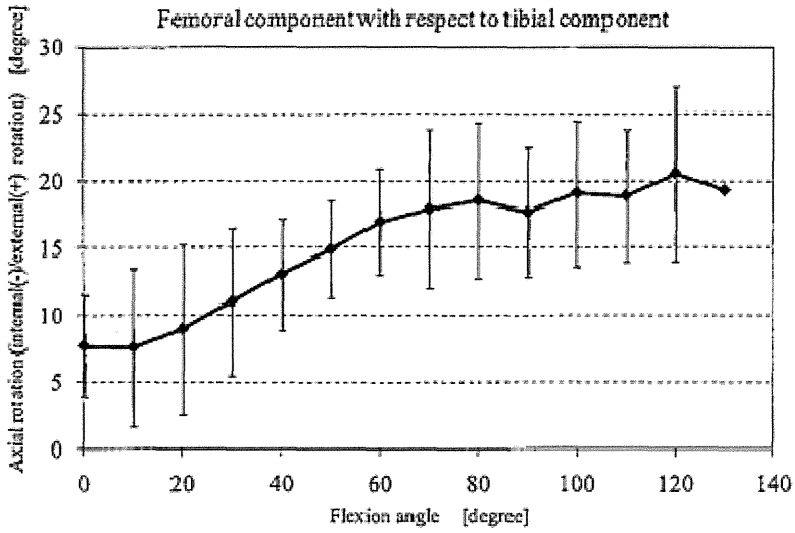

Figure 7. Axial rotation (internal/external rotation) of femoral component with respect to tibial component.

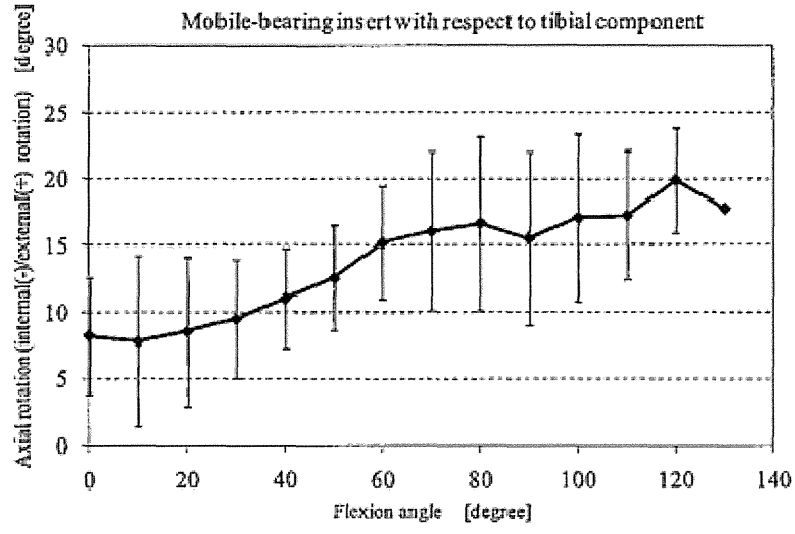

Figure 8. Axial rotation (internal/external rotation) of mobile-bearing insert with respect to tibial component.

4. DISCUSSION AND CONCLUSIONS

This study presented a procedure and the accuracy for 3D kinematic analysis of mobile-bearing insert in TKA using X-ray fluoroscopy, and finally performed clinical applications. Although it is difficult to obtain 3D kinematics of the polyethylene mobile-bearing insert because the polyethylene insert is transparent during fluoroscopy, accurate measurement of the insert can be achieved by tracking previously inserted tantalum beads using a specially designed insertion device. Utilizing the inserted beads information (position and orientation) and present feature-based 2D/3D registration technique, the 3D pose estimation of the mobile-bearing insert was successfully performed.

The accuracy validation of the 3D pose estimation for the mobile-bearing insert was performed by two experiments, which has not been reported in previous studies. The accuracy of the pose estimation depended on the orientation pattern of the insert, and the errors of z (medial-lateral) translation were large due to use of single-plane X-ray image (Table 1). However, the difference of the error by beads projection number (three or four beads) was relatively small, and also even if positional errors within 0.5mm were given for three or four strategically placed beads, the accuracy of present technique was found to be sufficient for analyzing mobile-bearing TKA kinematics.

In the clinical applications, for seven TKA patients, relative axial rotations of three components (femoral component, tibial component, and mobile-bearing insert) were determined. The results showed that the mobile-bearing insert was primary rotating relative to the tibial component rather than the femoral component. Therefore, as the femoral component axially rotated, the mobile-bearing insert was rotating a similar magnitude in the same direction (Figure 7 and 8). While, in a few case, the femoral component showed more external rotation than the mobile-bearing insert with respect to the tibial component during flexion. This maybe indicates the femoral component was sliding on the mobile-bearing insert during flexion. Thus, present technique enables us to better understand mobile-bearing TKA kinematics. Consequently, this type of evaluation is thought to be helpful for improving implant design and optimizing TKA surgical techniques.

AKNOWLEDGMENTS

This study was supported in part by the Global COE Program "in silico medicine" at Osaka University.

REFERENCES

[1] Banks, S.A., Hodge, W.A., "Accurate measurement of three-dimensional knee replacement kinematics using single-plane fluoroscopy," IEEE Trans. Biomed. Eng. 43, 638-649 (1996).
[2] Zuffi, S., Leardini, A., Catani, F., Fantozzi, S., Cappello, A., "A model-based method for the reconstruction of total knee replacement kinematics," IEEE Trans. Meg. Imag. 18, 981-991 (1999).
[3] Mahfouz, M.R., Hoff, W.A., Komistek, R.D., Dennis, D.A., "A robust method for registration of three-dimensional knee implant models to two-dimensional fluoroscopy images," IEEE Trans. Meg. Imag. 22, 1561-1574 (2003).
[4] Yamazaki, T., Watanabe, T., Nakajima, Y., Sugamoto, K., Tomita, T., Yoshikawa, H., Tamura, S., "Improvement of depth position in 2-D/3-D registration of knee implants using single-plane fluoroscopy," IEEE Trans. Meg. Imag. 23, 602-612 (2004).
[5] Fantozzi, S., Leardini, A., Banks, S.A., Marcacci, M., Giannini, S., Cantani, F., "Dynamic in-vivo tibio-femoral and bearing motions in mobile bearing knee arthroplasty," Knee Surg. Sports Traumatol. Arthrosc. 12, 144-151 (2004).
[6] Komistek, R.D., Dennis, D.A., Mahfouz, M.R., Walker, S., Outten, J., "In vivo polyethylene bearing mobility is maintained in posterior stabilized total knee arthroplasty," Clin. Orthop. Relat. Res. 428, 207-213 (2004).
[7] Weng, J., Cohen, P., Herniou, M., "Camera calibration with distortion models and accuracy evaluation," IEEE Trans. Pattern Anal. Machine Intell. 14, 965-980 (1992).
[8] Luenberger, D.G., [Linear and Nonlinear Programming], Addison-Wesley, Facsimile Edition, Massachusetts (1984).
[9] Canny, J., "A Computational Approach to Edge Detection," IEEE Trans. Pattern Anal. Machine Intell. 8, 679-698 (1986).
[10] Grood, E.S., Suntay, W.J., "A joint coordinate system for the clinical description of three-dimensional motions: Application to the knee," J. Biomech. Eng. 105, 136-144 (1983).

幼児期発症の側彎変形に対するDSB(愛称プレーリーくん)による治療の試み(第一報)

The Dynamic Spinal Brace (Nick name : Prairie) used in the treatment for the infante with spinal deformity : A preliminary report.

大阪発達総合療育センター南大阪療育園
梶浦　一郎

大阪大学大学院　器官制御外科学
森口　悠

はじめに

幼児期（6歳未満）に発症する脊柱側弯変形には乳児期突発性側弯，先天性側弯，症候性側弯があるとされている．今回6歳未満でDynamic Spinal Braceを用いて治療を開始した症候性側弯22例について報告する．

DSB(愛称プレーリーくん)について

側弯の治療に用いる体幹装具は1958年にMilwaukee Braceが報告されて以来基本的概念は殆ど変らない．その装着の困難さから最近は殆どunderarm型が用いられている[4]．硬質の骨盤帯を基礎として強力な矯正力と固定により有効とされているが特に脳性麻痺児などの症候性側弯には装着困難な例が多い．そこで我々は固定ではなく動的な矯正力と体幹の立ち直り機能を促進する装具を新たに作製した．支柱はポリカーボネイト製で，弾力を有して上部胸郭と骨盤外側面（腸骨稜ではない）とハンプ押えによる三点支持の原理により弾力的な矯正力の働くことを目的としたものであり，その基本理念から動的体幹装具(Dynamic Spinal Brace）と名付けた[3]．腸骨稜を避けることにより，同部に多く見られた皮膚障害（痛み，発赤）は殆ど無くなったが，装着中に装具が回旋することが起こりやすい欠点が判明した（DSB Ⅱ型）（図1）．そこで両大臀筋部を対称的に押える翼を加えることにより，安定して装着できるようになった（DSB Ⅲ型）．

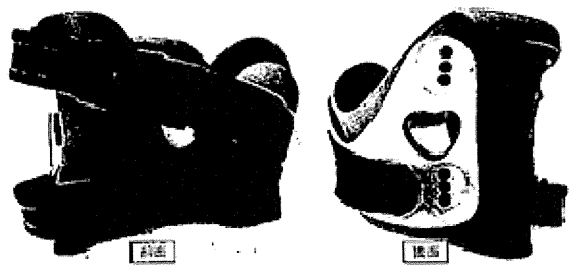

図1．DSB Ⅱ型の特徴
- 弾性のある3点支持．“固定”ではなく“たわみ”を利用する
- 装着時間は“状態に応じて徐々に延長する”
- 接触面積が少なく，軽量である．

特許番号　4747327

症例の概要

年齢は1歳～5歳（平均2.8歳）であり男

Key words：幼児期（Infante），症候性側弯(symptomatic Scoliosis)，DSB（Dynamic spinal Brace).

9例・女15例，計24例ある．基礎疾患は（表1）に示す如く多種にわたる中枢神経障害であった．側弯変形の様式はSingle curve 22例（右凸12例，左凸10例），Double curve 2例（胸椎右凸1例，胸椎左凸1例）であった．Cobb角については，Singleは21°～63°（平均39.7° ± 17.2°），Doubleは30/18，26/36（平均28/27）であった．

表1．症例の実際

男　9例	年齢：1才～5才（平均2．8才）
女　15例	
計　24例	観察期間：12ヶ月～30ヶ月（平均21．2ヶ月）

基礎疾患

脳性麻痺		8例
てんかん性脳症		3例
水頭症		3例
染色体・遺伝子異常		10例
マルファン症候群	色素失調	
ラルセン症候群	ダウン症候群	
グルタル酸尿症1型		
染色体8番，12番，13番，18番異常		
46XX,der(II)(11;17)(P15.5;q25)		

[症例1，Y.S　12番染色体異常]

1歳3か月の時点ですでに座位にてCobb角38°を示し，DSBを用いたが2歳5か月でCobb角60°に達している．2歳9か月時点でDSB装着してもCobb角48°を示し独歩可能となったが，今後の慎重な追跡が必要である[5),6)]．

[症例2，K.R　第8番染色体異常]（図2）

2歳時点でCobb角68°に達していてDSB治療開始．4歳3か月でCobb角46°にまで改善し，DSB装着すると更に20°にまで改善し座位可能になっている．

[症例3　O.M　染色体異常]

2歳8か月Cobb角63°を示し，3歳7か月の時点で急速に増悪し74°に達している．DSB装着するもCobb角78°と全く効果なしで，早急に手術治療を期待している．

結　果

DSB装着によるCobb角の変化をSingle curve 22例について見ると，DSBを装着してもその期間ですでに進行するものもみられたが平均ではほとんど変化していない。22例中10例は5°以上増悪した（図3）．一方で同じCobb角を維持できたものと，5°以上改善した例が合計12例あった．最終時のDSB装着時のCobb角は1例を除いて全てが50°以下であった．基礎疾患別の側弯の特徴は例数が少ないので見出せなかった．頂椎の位置による効果の違いは明らかに腰椎部の方が改善が多く見られた．治療開始前のCobb角と初期改善率との間には優位な相関があり（$P<0.05$），Cobb角が小さいほど初期改善率は高かった（図4）．

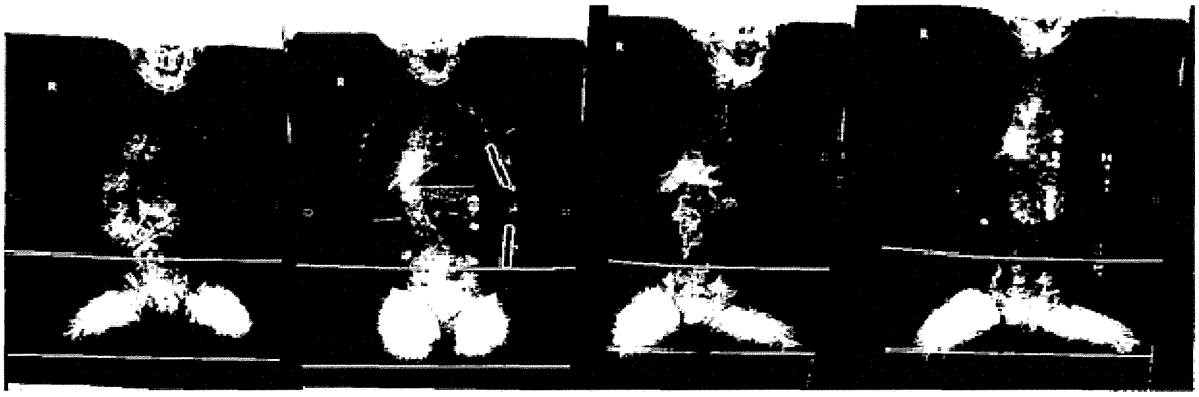

21年2月　68°　21年3月　35°　23年5月　46°　23年5月　20°

図2．症例2の各年のレ線像変化

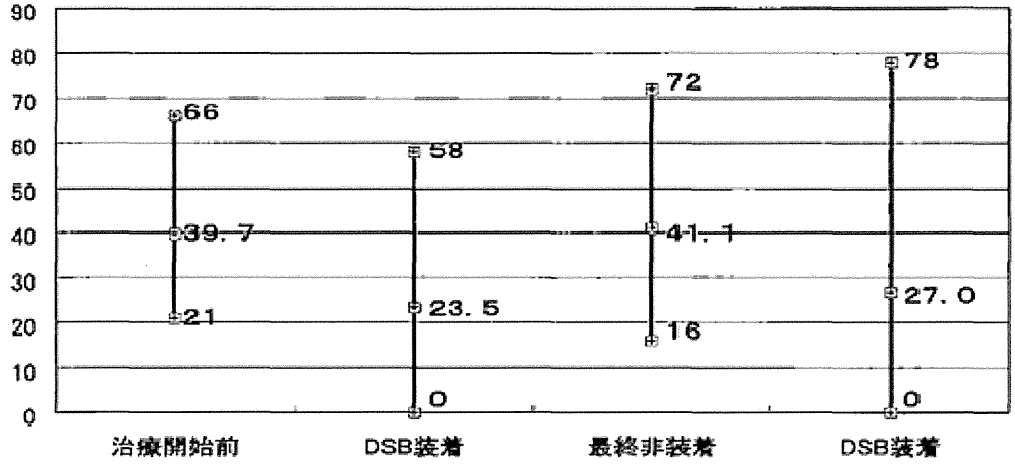

図３．DSBによる治療効果（Cobb角の変化）

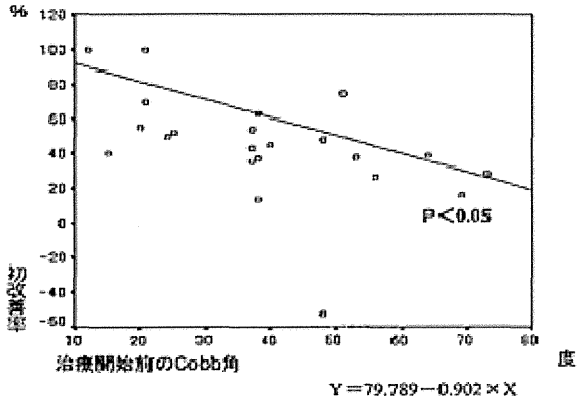

図４．DSBの効果

考　　察

脳性麻痺などの中枢神経障害にみられる症候性側弯は従来の各種装具ではあまり有効でない，と同時にADLの大きな妨げになるなどのため治療の継続が困難であり，最も有効な方法は手術療法とされていた[1]．特に乳児期にはギプス，牽引，装具が用いられているが苦痛を伴うことが多く，そのうえ呼吸嚥下障害，てんかん発作など全身状態に問題が多い例では危険を伴うと考えられた[2]．DSBでは全身状態の観察が十分できない夜間の装着は原則として禁止しているが，装着時間は介助者の意志に任せている．しかし装着時間は平均8.6時間（4時間～22時間）であるのは，装着に伴う苦痛が少ないためと考えられる．幼児期におけるDSBの主な使用目的は脊柱変形の改善と進行予防であるが，運動発達を促すPT，OTとの相乗効果，座位保持装置などの補助器具の簡素化，日常生活の便利さ（介護の容易，上肢の使用促進）も目的としている．

ま　と　め

６歳未満の時期での脊柱変形は確定していないものが多く，抗重力機能の未熟のための単なる不安定性も見られ，装具の効果は容易には判定できない．しかしこの年代においてもCobb角が大きい例は改善が困難な例もあり，出来ればCobb角が小さい時に装具治療を開始するのが望ましい．日常生活での介助も容易で（抱きやすい・食事がさせやすい・座らせやすい等），運動療法を行いやすく，効果も持続しやすい．これらのことはこの装具のコンプライアンスが良いことが大いに関係していると思われるので幼児からのこの装具の着用は有用と思われる（表２）．しかし，このような幼少からの側弯治療の効果は成長と大いに関係するので，今後なお長期観察を続けて判定することが重要である．

表2．DSBの主な使用目的

1．脊柱変形の矯正
2．脊柱変形の進行予防
3．運動発達のためのOT・PTとの相乗効果
4．座位保持装置などの補助具の簡便化
5．日常生活の便利さ（座位・立位・歩行器・上肢の使用促進・摂食嚥下の改善・介護の容易）

文　献

1）荒尾和彦，他：重複障害児に合併する側彎と装具療法．総合リハ，25：37－39，1997.
2）James O. Sandres, et al : Derotational Casting for Progressive Infantile Scoliosis. J Pediatr Orthop, 29 : 581-587, 2009.
3）梶浦一郎，他：脳性麻痺にみられる側彎に対する新しい装具（Dynamic Spinal Brace）による治療報告（第1報）．日本側弯症学会，24：65－69，1，2009.
4）Merv Letts, et al : Soft Boston Orthosis in Management of Neuromuscular Scoliosis : A Preliminarry Report. J Pediatr Orthop, 12 : 470-474, 1992.
5）盛島利文，他：乳幼児期の側弯症保存療法の検討．日小整会誌，18：289－293，2009.
6）盛島利文，他：当園における10歳未満発症の突発性側彎症の経過．J Jpn Scol Soc, 16 : 68-71, 2001.
7）辻太一，他：脊柱側弯症に対する治療，その中における装具療法　側弯症の基礎．日本義肢装具学会誌，25：177－183，2009.

3D Spine Kinematics on Riding Fitness Machines Using 2D/3D Image Registration

T. Yamazaki[1,2], Y. Nagamoto[3], H. Sakaura[4], D. Maeda[5], H. Yoshikawa[4] and K. Sugamoto[3]

[1] The Center for Advanced Medical Engineering and Informatics, Osaka University, Osaka, Japan
[2] Division of Image Analysis, Osaka University Graduate School of Medicine, Osaka, Japan
[3] Division of Orthopaedic Biomaterial Science, Osaka University Graduate School of Medicine, Osaka, Japan
[4] Department of Orthopaedics, Osaka University Graduate School of Medicine, Osaka, Japan
[5] Department of Radiology, Osaka University Hospital, Osaka, Japan

Abstract— **To achieve 3D kinematic analysis of total joint arthroplasty, 2D/3D image registration techniques have attracted attention in recent years. This study presents a 3D spine kinematic measurement method on riding fitness machines using a 2D/3D image registration. First, in order to create the 3D bone model of each spine, CT scan data from a healthy volunteer are used. Next, under fluoroscopic surveillance in the frontal and lateral planes, dynamic spine motions on riding fitness machines are recorded as serial digital x-ray images. 3D poses of each spine are estimated using a feature-based 2D/3D image registration which uses two directional fluoroscopic images and 3D surface model of spine, and finally the 3D kinematics are determined and visualized. In order to validate the accuracy of pose estimation for each spine using a feature-based 2D/3D image registration, computer simulation test was performed. The result showed that the root mean square errors were within 1.0 mm, 1.0 degree for all translations and rotations. In the clinical application 3D spine kinematic analysis using two type of riding fitness machines was successfully performed, and as the results the dynamic movement showed a smooth and reasonable physiologic pattern of motion.**

Keywords— **3D spine kinematics, 2D/3D image registration, Accuracy, X-ray fluoroscopy, Riding fitness machine.**

I. Introduction

To materialize 3D kinematic analysis of various joint including artificial joint implants, previous works have reported some different techniques for measuring the 3D joint kinematics. Video-based motion analysis techniques of skin-mounted markers has been used widely to study gross body motion but less to study detailed joint motion due to the problem of artefacts of skin and soft tissue movement. While, existing accurate 3D measurement techniques, such as computed tomography (CT) and magnetic resonance imaging (MRI), allow assessing movements of the underlying joint directly. However, CT and MRI are not yet capable of achieving high frame rates required for estimating dynamic joint motion, and also the restrictions imposed by the imaging environment (typically a small-diameter cylindrical space) prevent full-motion kinematics measurements.

To eliminate these problems, for kinematic measurement of artificial joint implants, researchers have recently used 3D pose estimation techniques called 2D/3D image registration [1-4], which determine the spatial position and orientation for metallic implants components (e.g. knee, hip, and elbow implants components [5-7]) from X-ray fluoroscopic images and computer aided design (CAD) models of the implants. For normal bones kinematics without artificial joint implants, although a CAD model of the bones is not readily available from the manufacturer, the model can be obtained CT or MRI scan data. Therefore, 3D pose estimation of the normal bones can be achieved. This study presents a 3D spine kinematic measurement method on riding fitness machines using a 2D/3D image registration. We also validate the accuracy of pose estimation for each spine by computer simulation test, and apply the method to dynamic 3D spine kinematic analysis on riding fitness machines.

II. Materials and Metods

A. Condition and requirement

To achieve 3D pose estimation of normal spine using X-ray fluoroscopic images, it is necessary to have an accurate geometrical model of each spine (thoracic, lumbar, and sacral) and to know the geometrical parameters of the X-ray imaging system.

The 3D geometry of each spine is taken from CT scan data. Multidetector computed tomography (MDCT) data, the 0.63 mm axial slice with 512 x 512 image matrix, from a healthy volunteer was used to create 3D bone surface models of thoracic, lumbar, and sacral spine. Segmentation of the bone was performed by applying a thresholding filter. Fig. 1 shows a 3D surface model of normal spine.

The geometrical parameters of the imaging system are determined with a 3D calibration cube and a non-linear calibration technique [8]. The calibration cube has evenly spaced 129 metallic markers, which are employed as calibration markers.

M. Long (Ed.): World Congress on Medical Physics and Biomedical Engineering, IFMBE Proceedings 39, pp. 223–225, 2012.
www.springerlink.com

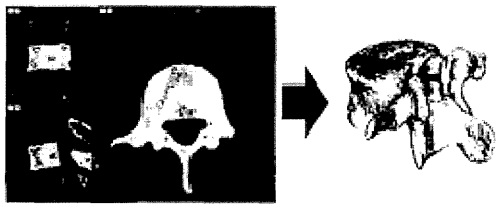

Fig. 1 A spine segmentation and its 3D surface model.

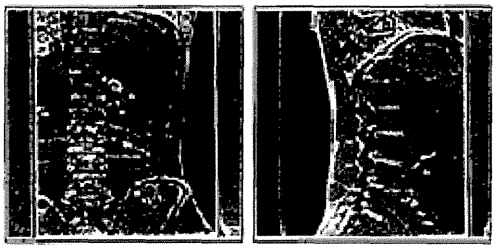

Fig. 2 Frontal and lateral dynamic FPD images of the spine.

B. Image acquisition and processing

Under fluoroscopic surveillance in the frontal and lateral planes, dynamic spine motions on a riding fitness machine were separately recorded as serial digital X-ray images (1024 x 1024 x 12 bits/pixels, 7.5Hz serial spot images as a DICOM file) using a 17-inch dynamic flat-panel detector (FPD) system (C-vision, Shimadzu). This means that two directional X-ray images (approximate bi-plane images) are used to accurately estimate 3D poses of each spine model. To extract the contours of each spine from the acquired image, a Canny's edge detector was applied [9]. Generally, the edges of a fluoroscopic bone image are not sharp like with a metallic implant because of the low contrast of the material. However, use of dynamic FPD images enabled us to easily detect bone edges. False edges and noises detected were manually erased, and the obtained contours were utilized to estimate the 3D pose of the spine model. Fig. 2 shows the frontal and lateral dynamic FPD images of the spine.

C. 2D/3D image registration

3D poses of each spine are estimated using a feature-based 2D/3D image registration [2,4], which uses two directional FPD image contours and 3D bone surface model of each spine. The basic principle of this algorithm is that the 3D pose of a model can be determined by projecting rays from contour points in an image back to the X-ray focus and noting that all of these rays are tangential to the model surface (Fig. 3). Therefore, 3D poses are estimated by minimizing the sum of Euclidean distances between all projected rays and the model surface. A cost function E is defined as the sum of Euclidean distance d_i from point $\mathbf{q}_i$ on the projection rays (corresponding to the point $\boldsymbol{p}_i$ on the contours) to the closest point s_i on the model surface.

$$E = \sum_{i=1}^{N} d_i^2 \tag{1}$$

The distance d_i is given by

$$d_i = \pm|\mathbf{q}_i - \mathbf{s}_i| \tag{2}$$

where $0 \le i < N$ and N is the number of contour points in the frontal or lateral X-ray images. Negative values indicate rays that cross the model surface. Thus, from single-plane X-ray images, the 3D poses of each spine model are estimated by minimizing the cost function E (equation (1)) iteratively using a nonlinear optimization technique [10]. A good function for determining convergence of the 3D pose of the model from single-plane X-ray images is given by root mean square distance (RMSD):

$$\mathrm{RMSD} = \sqrt{\sum_{i=0}^{N} d_i^2 \Big/ N} \tag{3}$$

Finally, the 3D poses of each spine model are estimated by minimizing the sum of two cost functions using approximate bi-plane images (frontal and lateral images).

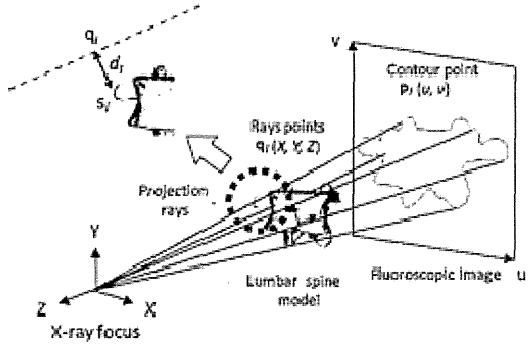

Fig. 3 3D pose estimation of each spine model from a dynamic FPD image.

III. Experimental results

A. Computer simulation test

In order to validate the accuracy of pose estimation for each spine using a feature-based 2D/3D image registration, computer simulation test was performed. A set of 3 synthetic silhouette images from the frontal and lateral directions was created for each lumbar spine model (L1~L5) in known typical orientations. Ten initial guess poses of each spine model were randomly given from within ±5 mm and ±5 degree of the correct value. Errors in the 3D pose of the model were determined by comparing the estimated pose to the known pose. Fig. 4 shows representative lumbar spine images from the frontal and lateral directions used for computer simulation test.

The results of the computer simulation test are summarized in Table 1. The root-mean-square errors are given for each lumbar spine model (L1~L5). For each spine model, the error of all translations and rotations were within 1.0 mm and 1.0 degree, respectively. For translations, the error of the translation Y was smaller, and for rotations, the error of the rotation X and Z were comparatively smaller. In addition, there were no so differences between the errors of each spine model (L1~L5).

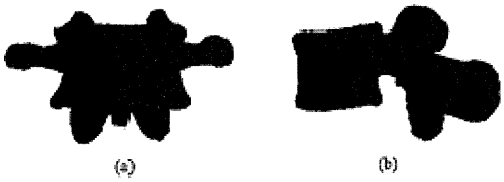

Fig. 4 Representative lumber spine images used for computer simulation test. (a) frontal view, (b) lateral view.

Table 1 Root-mean-square errors of 3D pose estimation for each lumbar spine model (L1-L5) by computer simulation test.

	Translation (mm)			Rotation (degrees)		
	X	*Y*	*Z*	*X*	*Y*	*Z*
L1	0.50	0.16	0.50	0.29	0.68	0.37
L2	0.73	0.20	0.59	0.23	0.61	0.54
L3	0.98	0.11	0.50	0.20	0.65	0.48
L4	0.73	0.17	0.53	0.17	0.50	0.34
L5	0.91	0.19	0.52	0.21	0.49	0.52

B. Clinical application

We applied the present method to dynamic 3D spine kinematic analysis on riding fitness machines. Experiments were performed using two type of riding fitness machines, products A (JOBA EU7800, Panasonic Electric Works) and B (RODEOBOY2, Thrive). Both of products A and B are designed to reproduce motions of a figure of eight, respectively. A healthy male subject gave informed consent to participate in this study, and the study was approved by the authors' Institutional Review Board. 3D kinematics from twelfth thoracic to first sacral spine (total seven vertebras) were determined and visualized.

As the results of the 3D spine kinematics, Fig. 5 visualizes tip motions of the spinous process of thoracic, lumbar, and sacral vertebras from axial view for products A and B, respectively. The spine kinematics of product A clearly showed motions of a figure of eight according to the design concept, but that of product B was not observed as motions of a figure of eight. In addition, the spine kinematics of product A exhibited large lateral bending and axial rotation compared with that of product B as shown in Fig. 6 and 7.

Fig. 5 Tip motions of the spinous process of the vertebras from axial view for products A and B.

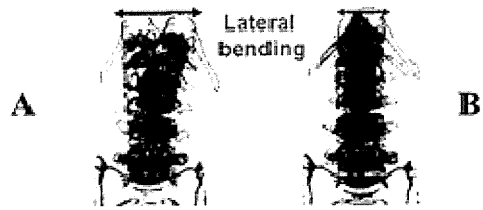

Fig. 6 Lateral bending of the spine for products A and B.

Fig. 7 Axial rotation of the spine for products A and B.

IV. Discussion and Conclusions

This study presented a 3D spine kinematic measurement method on riding fitness machines using a feature-based 2D/3D image registration. Utilizing two directional dynamic FPD images (approximate bi-plane images), 3D determination of the spine kinematics was successfully performed.

In computer simulation test, the accuracy of pose estimation for each lumbar spine (L1~L5) were validated, and the error of all translations and rotations were within 1.0 mm and 1.0 degree. Thus, the accuracy of present method was found to be sufficient for analyzing 3D spine kinematics.

In the result of clinical application using two type of riding fitness machines (products **A** and **B**), the spine kinematics of product **A** clearly showed motions of a figure of eight according to the design concept, and then exhibited large lateral bending and axial rotations during spine motions. These large motions might be caused by motions of a figure of eight. Consequently, this type of evaluation is thought to be helpful for developing health and welfare device and assessing its safety and efficiency. As a future work, we are planning to quantitative assessment of 3D spine kinematics including normal joint, joint diseases and dysfunction.

References

1. Banks SA, Hodge WA (1996) Accurate measurement of three-dimensional knee replacement kinematics using single-plane fluoroscopy. IEEE Trans Biomed Eng 43:638-649
2. Zuffi S, Leardini A, Catani F, et al. (1999) A model-based method for the reconstruction of total knee replacement kinematics. IEEE Trans Med Imag 18:981-991
3. Mahfouz MR, Hoff WA, Komistek RD, et al. (2003) A robust method for registration of three-dimensional knee implant models to two-dimensional fluoroscopy images. IEEE Trans Meg Imag 22:1561-1574
4. Yamazaki T, Watanabe T, Nakajima Y, et al. (2004) Improvement of depth position in 2-D/3-D registration of knee implants using single-plane fluoroscopy. IEEE Trans Med Imag 23:602-612
5. Tamaki M, Tomita T, Watanabe T, et al. (2009) In vivo kinematic analysis of a high-flexion, posterior-stabilized, mobile-bearing knee prosthesis in deep knee-bending motion. The Journal of Arthroplasty 24:972-978
6. Koyanagi J, Sakai T, Yamazaki T, et al. (2011) In vivo kinematic analysis of squatting after total hip arthroplasty. Clin Biomech 26:477-483
7. Futai K, Tomita T, Yamazaki T, et al. (2010) In vivo three-dimensional kinematics of total elbow arthroplasty using fluoroscopic imaging. International Orthopaedics 34:847-854
8. Weng J, Cohen P, and Herniou M (1992) Camera calibration with distortion models and accuracy evaluation. IEEE Trans Pattern Anal Machine Intell 14: 965-980
9. Canny J (1986) A computational approach to edge detection. IEEE Trans Pattern Anal Machine Intell 8:679-698
10. Luenberger DG (1984) Linear and Nonlinear Programming. Addison-Wesley, Facsimile edition, Massachusetts

Address of the corresponding author:

Author: Takaharu Yamazaki
Institute: Osaka University
Street: 2-2 Yamadaoka, Suita
City: Osaka
Country: Japan
Email: yamazaki@image.med.osaka-u.ac.jp

J Neurosurg Spine 17:327–333, 2012

Three-dimensional motion of the uncovertebral joint during head rotation

Clinical article

Yukitaka Nagamoto, M.D., Ph.D.,[1] Takahiro Ishii, M.D., Ph.D.,[2] Motoki Iwasaki, M.D., Ph.D.,[1] Hironobu Sakaura, M.D., Ph.D.,[3] Hisao Moritomo, M.D., Ph.D.,[1] Takahito Fujimori, M.D., Ph.D.,[1] Masafumi Kashii, M.D., Ph.D.,[1] Tsuyoshi Murase, M.D., Ph.D.,[1] Hideki Yoshikawa, M.D., Ph.D.,[1] and Kazuomi Sugamoto, M.D., Ph.D.[1]

[1]*Department of Orthopaedics, Osaka University Graduate School of Medicine;* [2]*Department of Orthopaedic Surgery, Kaizuka City Hospital, Osaka; and* [3]*Department of Orthopaedic Surgery, Kansai Rosai Hospital, Hyogo, Japan*

Object. The uncovertebral joints are peculiar but clinically important anatomical structures of the cervical vertebrae. In the aged or degenerative cervical spine, osteophytes arising from an uncovertebral joint can cause cervical radiculopathy, often necessitating decompression surgery. Although these joints are believed to bear some relationship to head rotation, how the uncovertebral joints work during head rotation remains unclear. The purpose of this study is to elucidate 3D motion of the uncovertebral joints during head rotation.

Methods. Study participants were 10 healthy volunteers who underwent 3D MRI of the cervical spine in 11 positions during head rotation: neutral (0°) and 15° increments to maximal head rotation on each side (left and right). Relative motions of the cervical spine were calculated by automatically superimposing a segmented 3D MR image of the vertebra in the neutral position over images of each position using the volume registration method. The 3D intervertebral motions of all 10 volunteers were standardized, and the 3D motion of uncovertebral joints was visualized on animations using data for the standardized motion. Inferred contact areas of uncovertebral joints were also calculated using a proximity mapping technique.

Results. The 3D animation of uncovertebral joints during head rotation showed that the joints alternate between contact and separation. Inferred contact areas of uncovertebral joints were situated directly lateral at the middle cervical spine and dorsolateral at the lower cervical spine. With increasing angle of rotation, inferred contact areas increased in the middle cervical spine, whereas areas in the lower cervical spine slightly decreased.

Conclusions. In this study, the 3D motions of uncovertebral joints during head rotation were depicted precisely for the first time.
(http://thejns.org/doi/abs/10.3171/2012.6.SPINE11104)

Key Words • **uncovertebral joint** • **three-dimensional kinematics** • **head rotation** • **volume registration** • **cervical**

The uncovertebral joints (Luschka joints) are small but clinically important anatomical structures of the cervical vertebrae. Each joint consists of the uncinate process and corresponding recess located on the inferolateral surface of the superior adjacent vertebral body. In the aged or degenerative cervical spine, osteophytes arising from an uncovertebral joint can cause cervical radiculopathy, often requiring decompression surgery. Although the biomechanical roles[1,15,18,19,28] and morphological characteristics[4,6,14,17] of the uncovertebral joints have been investigated, the functions of uncovertebral joints have yet to be definitively clarified. Full elucidation of the function, including kinematics, of the uncovertebral joints is thus very important.

According to previous comparative anatomical investigations, uncinate processes are found only in ob-

This article contains some figures that are displayed in color online but in black-and-white in the print edition.

ligate or facultative bipedal animals, such as primates, marsupials, and rodents.[7] In the upright position, rotation of the cervical spine is needed to allow the animal to look around. From this anatomical observation, uncovertebral joints are believed to play some role in head rotation.[17,19] To the best of our knowledge, however, no studies have reported kinematics of the uncovertebral joints during head rotation. We have developed a 3D imaging system to noninvasively evaluate relative motions of individual cervical vertebrae in vivo.[8–10] The purpose of this study was to elucidate 3D motion of the uncovertebral joints to provide a better understanding of the function of these joints during head rotation.

Methods

Study Population

Study participants were 10 healthy volunteers (5 men and 5 women) with neither neck pain nor a medical history of cervical spine disorders. Mean age at the time of imaging was 25.1 years (range 22–31 years). All study protocols were approved by the institutional review board. Informed consent was obtained in all volunteers.

Acquisition of 3D MRI

Each volunteer was placed supine on the MRI table and underwent 3D MRI in 11 positions with the head rotated: 0° (neutral), 15°, 30°, 45°, and 60°, and maximum rotation to each side (left and right). We instructed all volunteers to rotate the head as perpendicularly as possible about the axis of the body trunk. The shoulders of each volunteer were fixed to the table using a band. All 3D MRI scans were acquired using a 1.0-T commercial MRI system (Signa LX, General Electric) in conjunction with a torso-phased array coil. A 3D fast-gradient recalled acquisition in the steady state (GRASS) sequence was used (TR 8.0 msec, TE 3.3 msec, slice thickness 1.5 mm, no interslice gap, flip angle 10°, FOV 24 cm, inplane acquisition matrix 256 × 224). Magnetic resonance imaging data were saved in DICOM format and transmitted to a computer workstation, where image processing was performed using software developed in our laboratory (Virtual Place M series, Medical Imaging Laboratory).

Motion Analysis

Our original method used in the present study has been fully described in previous reports[8–10] and will be described here only briefly. First, regions of interest were extracted in 3D from the 3D MRI data (segmentation) and 6 vertebrae from C-2 to C-7 were extracted semiautomatically using an intensity threshold technique. Second, using a volume registration method,[8–10] 3D motions of each vertebra in an absolute coordinate system were calculated by automatically superimposing the segmented region of each vertebra on 3D MRI in the neutral position over images of every position. Intervertebral motions of every motion segment from C2–3 to C6–7 were then calculated by converting the absolute motion (3 × 4 matrix) obtained from the preceding image processing into a relative motion with respect to the subjacent vertebra. These motions were expressed in 6 df by Euler angles with the sequence of pitch (X), yaw (Y), roll (Z), and translations using a previously defined anatomical coordinate system.[8–10] Accuracy of this method was as follows: 0.24° for flexion-extension, 0.31° for lateral bending, 0.43° for axial rotation, 0.52 mm for superoinferior translation, 0.51 mm for anteroposterior translation, and 0.41 mm for lateral translation, as described in detail previously.[10]

Creation of 3D Bone Models

Surface bone models constructed from 3D MRI data provided insufficient information on configuration to investigate in vivo 3D kinematics of the uncovertebral joint, due to a lack of spatial resolution. We therefore decided to choose surface bone models from multidetector row CT (LightSpeed 16, General Electric) for analysis, and these models reproduced anatomical structures much more accurately than models from 3D MRI. Computed tomography data for the cervical spine were selected from the DICOM server at our institution, based on anatomical characteristics described in several studies of the uncovertebral joints.[4,6,14,17,18] The source of the data was a 28-year-old man who was not part of the 10-patient cohort. More specifically, characteristics of the selected CT data were as follows: the uncinate processes situated laterally at middle cervical levels (C2–3, C3–4, C4–5) and dorsolaterally at lower cervical levels (C5–6, C6–7)[6,17] demonstrated reduced height of the processes in relation to the vertebral bodies at lower cervical levels (Fig. 1).[4,14] Regarding sagittal orientation of facets, facet slope is more gradual as the cervical level descends caudally. There were no degenerative changes, and normal disc heights were maintained at all levels on conventional 2D MRI. In this way, 6 surface bone models from C-2 to C-7 were created.

Three-Dimensional Visualization of Motion

All intervertebral motions from the 10 volunteers were aggregated and standardized at every intervertebral level using our original operation algorithm. The results of standardized 3D intervertebral motions were expressed as matrices. A pair of CT vertebral models of a functional spinal unit was displayed in virtual 3D space, allowing us to obtain a 3D movie of intervertebral motions by introducing the matrices to the superior adjacent vertebra alone and keeping the subjacent vertebra fixed (Fig. 2, Video 1).

> Video 1. Clip showing 3D motion of the uncovertebral joints. This 3D animation of the uncovertebral joints during head rotation shows joints alternating between contact and separation accompanying torsion of the intervertebral space. To allow a better understanding of intervertebral motions, the subjacent vertebra is always fixed in this clip. For example, C-3 is fixed in the clip showing C2–3. Click here to view with Media Player. Click here to view with Quicktime.

Creation of the animation was accomplished using originally developed software (Orthopedics Viewer, Osaka University) that allowed the observer to closely examine every uncovertebral joint from every observation point needed. These 3D animations helped us to better understand the joint kinematics.

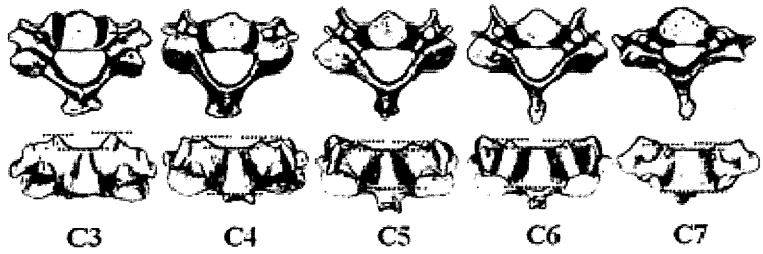

FIG. 1. Surface bone models created using CT data. We chose CT data with the following anatomical characteristics: uncinate processes situated laterally at middle cervical levels (C3–4) and dorsolaterally at lower cervical levels (C5–7), represented in the upper row as *dark gray* areas, as well as relatively reduced height of the processes at lower cervical levels, represented in the lower row as *dashed lines*.

Contact Area

We measured inferred contact areas of the uncovertebral joints during head rotation from bone surface models using a proximity mapping method.[16] Proximity mapping involves the visualization of distance from 1 bone to the nearest neighboring bone. We defined the area within a preset interbone distance as the inferred contact area. Contact areas were investigated at 15° increments during head rotation at every intervertebral level from C2–3 to C6–7 (Fig. 3, Video 2).

VIDEO 2. Clip showing inferred contact area of the uncovertebral joint. The inferred contact areas of the uncinate processes during head rotation were situated directly lateral at the middle cervical spine and dorsolateral at the lower cervical spine. Click here to view with Media Player. Click here to view with Quicktime.

Thresholds of preset interbone distances varied within 0.5–1.0 mm according to the individual joint size and intervertebral space.

Results

Intervertebral Motion

In main axial rotation, C4–5 and C5–6 were the most mobile segments and C2–3 was the least mobile segment, as previously reported (Table 1). During head rotation, larger rotation angles were observed in coupled lateral bending than in main axial rotation in all segments, and C2–3 and C3–4 were the most mobile segments in coupled lateral bending, despite the immobility in axial rotation (Table 2).

Behavior of Uncovertebral Joints

The 3D animation of uncovertebral joints during head rotation showed joints alternating between contact and separation accompanying torsion of the intervertebral space. On the side ipsilateral to head rotation, both joint surfaces were in contact with each other, while those on the contralateral side were separated (Fig. 2, Video

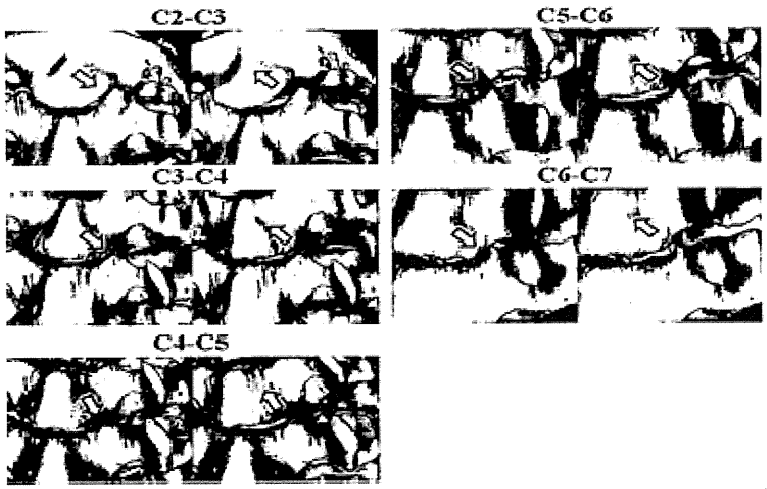

FIG. 2. The behaviors of uncovertebral joints were shown in a 3D animation. Each paired image focuses on the left uncovertebral joint from a left anterior oblique view. *Downward arrows* show contact and *upward arrows* show separation of the joint. For each level, left panels represent head rotation to the left, and right panels represent head rotation to the right.

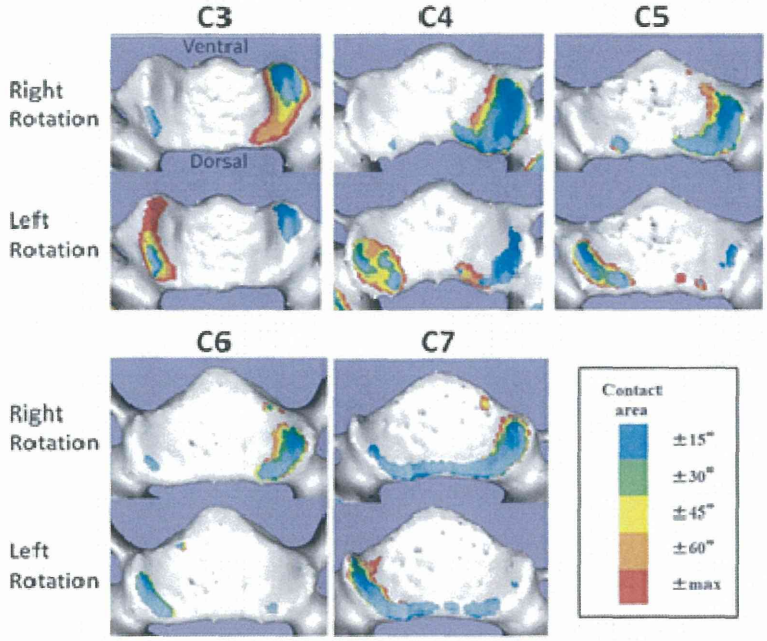

FIG. 3. Inferred contact areas projected on the uncinate process side. Each panel represents a cranial view with the upper part of each panel as the ventral side. Inferred contact areas are shown using 5 different colors, as shown in the key.

1). This pattern of motion was strongly apparent in the middle cervical spine, especially at the C2–3 level.

Contact Areas for Uncovertebral Joints

Inferred contact areas of the uncovertebral joints are shown in Fig. 3 and Video 2. Inferred contact areas showed that the uncovertebral joints were the first contact areas in the intervertebral space during head rotation and were situated directly lateral at the middle cervical spine and dorsolateral at the lower cervical spine. The dimensions (mm^2) of inferred contact areas were also calculated (Fig. 4). With increasing rotation angle of the head, inferred contact areas increased in the middle cervical spine, but slightly decreased in the lower cervical spine.

Discussion

Roles for Uncovertebral Joints and Uncinate Processes During Head Rotation

During head rotation, lateral flexion is coupled with rotation in the cervical spine and is called "coupled motion." Facet joints undoubtedly represent the biggest contributors to such motion, due to their oblique orientation.[9,18] In addition, several studies have suggested the contribution

TABLE 1: Intervertebral motion during head rotation: main axial rotation*

Head Rotation Angle (°)	C2–3	C3–4	C4–5	C5–6	C6–7
rt max	−2.3 ± 1.2	−4.7 ± 1.0	−4.9 ± 1.3	−4.5 ± 0.8	−2.8 ± 0.7
rt 60	−1.5 ± 0.9	−3.6 ± 0.8	−4.0 ± 1.2	−3.8 ± 0.6	−2.3 ± 0.5
rt 45	−0.7 ± 0.8	−2.3 ± 0.5	−2.7 ± 1.3	−2.9 ± 0.4	−2.0 ± 0.8
rt 30	−0.2 ± 0.7	−1.0 ± 0.7	−1.7 ± 1.1	−1.9 ± 0.7	−1.2 ± 0.9
rt 15	0.0 ± 0.7	−0.2 ± 0.5	−0.8 ± 0.5	−1.3 ± 0.7	−1.0 ± 0.9
lt 15	−0.4 ± 0.6	0.2 ± 0.7	0.9 ± 0.5	1.6 ± 1.2	0.7 ± 1.1
lt 30	0.2 ± 0.4	1.1 ± 0.9	1.4 ± 0.5	1.8 ± 1.4	1.0 ± 1.4
lt 45	0.4 ± 0.5	2.0 ± 0.9	2.1 ± 0.7	2.4 ± 1.4	1.2 ± 0.9
lt 60	1.1 ± 0.7	2.9 ± 1.0	3.1 ± 0.9	3.3 ± 1.5	2.1 ± 1.0
lt max	1.5 ± 0.6	3.8 ± 1.0	3.9 ± 1.1	4.0 ± 1.5	2.4 ± 0.9

* All values given in mean degrees ± SD. Negative values = right axial rotation; positive values = left axial rotation.

TABLE 2: Intervertebral motion during head rotation: coupled lateral bending*

Head Rotation Angle (°)	C2–3	C3–4	C4–5	C5–6	C6–7
rt max	4.0 ± 1.3	6.2 ± 1.1	5.7 ± 1.1	5.6 ± 1.2	4.9 ± 1.6
rt 60	2.5 ± 1.3	5.0 ± 1.2	4.4 ± 1.3	4.9 ± 1.1	3.6 ± 1.4
rt 45	0.6 ± 1.0	3.1 ± 1.2	3.5 ± 1.2	3.0 ± 1.2	2.5 ± 1.7
rt 30	−0.6 ± 1.7	1.8 ± 1.2	1.9 ± 1.0	2.4 ± 1.3	1.7 ± 1.9
rt 15	−0.9 ± 1.6	0.7 ± 0.9	1.3 ± 0.8	1.2 ± 1.5	1.3 ± 1.2
lt 15	1.4 ± 2.1	−0.4 ± 0.9	−1.7 ± 1.3	−1.2 ± 1.3	−1.6 ± 2.7
lt 30	0.4 ± 2.0	−1.4 ± 0.8	−1.6 ± 1.1	−2.2 ± 1.9	−1.2 ± 1.9
lt 45	−0.8 ± 2.2	−2.3 ± 0.8	−2.6 ± 0.8	−2.6 ± 1.7	−2.5 ± 2.0
lt 60	−2.0 ± 2.1	−3.7 ± 1.2	−3.7 ± 0.7	−3.7 ± 1.3	−3.1 ± 2.3
lt max	−3.5 ± 1.8	−5.0 ± 1.2	−4.8 ± 1.0	−4.6 ± 1.4	−4.3 ± 2.2

* All values given in mean degrees ± SD. Negative values = left lateral bending; positive values = right lateral bending.

of uncinate processes to coupled motion.[1,7,13,19] Hall[7] noted that among vertebrates, uncinate processes on the cervical vertebrae are found only in obligate or facultative bipeds, which require rotation of the neck to look around. Given these findings, he hypothesized that the uncovertebral joints arose during evolution from quadrupedalism to bipedalism, and bear some relationship to neck rotation. To verify Hall's hypothesis, Penning and Wilmink[19] calculated the axis of rotation from the anatomical shape of uncovertebral joints, using CT sections in the plane of the facet joints in 2 different positions. These authors showed that coupling of lateral bending and rotation of the middle and lower cervical spine might be explained exclusively by the axis and morphological structure of the uncovertebral joints, and that the uncinate processes are also essential for rotation. Clausen et al.[1] quantitatively investigated contributions of the uncovertebral joints to motion of a spinal segment, including axial rotation, for the first time. Using finite element models, they elucidated that the presence of the uncovertebral joint (a fissure) leads to increased motions, while the uncinate processes act as stabilizers with respect to motion of the cervical spinal segment, particularly during axial rotation and lateral bending of the cervical spine.[1] However, that study was performed using only computer simulations, and the acquired data were not derived from real sources. Moreover, they analyzed kinematics only at the C5–6 segment, whereas anatomical variations at different vertebral levels may influence cervical biomechanics.

In our study, with increasing angle of head rotation, two opposite surfaces of the uncovertebral joint became closer and closer on the ipsilateral side of rotation, while surfaces on the contralateral side became more and more separated. This pattern was strongly observed in the middle cervical spine. Moreover, at these levels, inferred contact areas were situated directly lateral and increased with increasing angle of rotation, particularly at C2–3. In the middle cervical spine, larger coupled lateral bending would accompany head rotation, as these levels show a steeper sagittal inclination of facets than those of the lower cervical spine.[11] Taking these findings together, we speculated that the presence of large processes relative to the vertebral body[14] might restrict excessive coupled lateral bending and disperse mechanical stresses effectively on large joint surfaces in the middle cervical spine. In fact, the C2–3 segment, which has the largest uncinate process, had the smallest motion in terms of both main axial rotation and coupled lateral bending in our study.

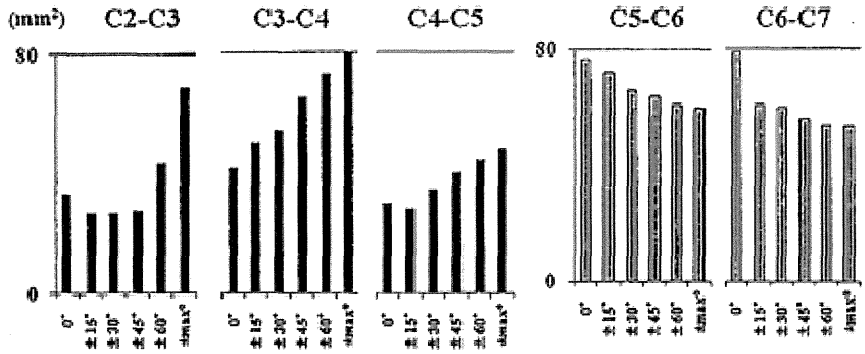

FIG. 4. Inferred contact areas (mm²) shown as means of right and left rotation at each intervertebral level, according to the angle of head rotation. With increasing rotation angle of the head, inferred contact areas increased in the middle cervical spine, but slightly decreased in the lower cervical spine.

Conversely, in the lower cervical spine, the inferred contact areas were situated dorsolaterally and these areas slightly decreased with increasing angle of rotation. Focusing only on the shape of the uncinate processes in the lower cervical spine, which displays more gradual inclination of facets than those of the middle cervical spine, axial rotation should be allowed without large coupled lateral bending. Therefore, the uncinate processes of the lower cervical spine might play a less important role in restricting excessive coupled lateral bending than those of the middle cervical spine. Given this observation, we speculated that uncinate processes of the lower cervical spine might not have to be as large as those of the middle cervical spine and instead play an important role in facilitating rotation of the cervical spine by placing the stress-focusing region on the posterolateral side of the upper surfaces of the vertebrae.

Nerve Root Compression and Uncovertebral Osteophytes in the Lower Cervical Spine

Cervical radiculopathy is often related to osteophyte formation around the uncinate process; C-7 root lesions are the most common, followed by C-6 lesions.[20,21] A longer course of the nerve root in close proximity to the uncovertebral joint may explain the predisposition toward nerve root compression by uncovertebral osteophytes at these levels.[5] However, anatomical or biomechanical reasons for a predisposition toward uncovertebral osteophytes in the lower cervical spine remain unclear.

In the present study, we elucidated that the uncovertebral joints are the first contact areas in the intervertebral space during head rotation. From these results, we speculated that as disc height diminishes with degeneration, earlier contact should occur around the uncovertebral joints during head rotation, and would be likely to promote age-related degenerative change around the uncovertebral joints due to the increased frequency of mechanical stress. If the degenerated disc causes abnormal intervertebral kinematics, further degenerative changes around the uncovertebral joints would occur. The lower cervical spine is well-known as the level most commonly affected by aging,[2,5,15,22] and moreover, inferred contact areas of the uncovertebral joints at the lower cervical spine were situated dorsolaterally and decreased with increasing angle of rotation. These contact areas are closer to the course of the nerve root than in the middle cervical spine and may be subjected to strong mechanical stress, because stresses are focused in such small areas. The accumulation of mechanical stress in joints induces osteophyte formation.[12] Head axial rotation movements are often repeated during activities of daily living.[23] Repeated head rotation in the course of activities of daily living might thus contribute to spur formation around contact areas of the uncovertebral joints in the lower cervical spine close to the intervertebral foramen. This speculative situation would account for the fact that cervical radiculopathy generally occurs in the lower cervical spine, particularly C5–6 and C6–7.

Limitations of the Study

Several limitations in this study must be addressed. First, information was obtained from animations (Videos 1 and 2) comprising only 11 different positions and could not be obtained with the volunteer in an upright position. Second, individual variability in uncovertebral joints6 could not be taken into account, even though these variations are likely to affect kinematics. Moreover, the surface bone models were constructed using data from a volunteer outside the 10-patient cohort. We acknowledge that this method includes the potential for bias. Third, contact areas of the uncovertebral joints were not "true" (verified), but were instead inferred. The presence of intervening tissues such as discs, joint cartilages, and synovial fluids were not taken into account. And fourth, contact pressure and pressure distributions could not be measured using our methods. Despite all these limitations, we believe that no other approaches currently allow the investigation of 3D motion of the uncovertebral joints in healthy individuals. The present study thus offers a step toward a better understanding of functions of the uncovertebral joints.

Conclusions

We have shown 3D motion of the uncovertebral joints during head rotation for the first time. Standardized 3D intervertebral motions of the cervical spine showed that the uncovertebral joints alternate between contact and separation during head rotation. Inferred contact areas of uncovertebral joints were situated directly lateral at the middle cervical spine and dorsolateral at the lower spine. With increasing angles of rotation, inferred contact areas increase in the middle cervical spine, particularly at C2–3, whereas areas slightly decrease in the lower cervical spine.

Disclosure

The authors report no conflict of interest concerning the materials or methods used in this study or the findings specified in this paper.

Author contributions to the study and manuscript preparation include the following. Conception and design: Nagamoto, Iwasaki, Moritomo. Acquisition of data: Nagamoto, Ishii. Analysis and interpretation of data: Nagamoto, Sakaura. Drafting the article: *Nagamoto. Critically revising the article: all authors.* Reviewed submitted version of manuscript: all authors. Approved the final version of the manuscript on behalf of all authors: Nagamoto. Administrative/technical/material support: Iwasaki, Murase, Yoshikawa, Sugamoto. Study supervision: Iwasaki, Murase, Yoshikawa, Sugamoto.

Acknowledgments

The authors thank Ryoji Nakao for assisting with software programming and Yoshihiro Sakaguchi for help with MRI.

References

1. Clausen JD, Goel VK, Traynelis VC, Scifert J: Uncinate processes and Luschka joints influence the biomechanics of the cervical spine: quantification using a finite element model of the C5-C6 segment. J Orthop Res 15:342–347, 1997
2. Dvorak J, Panjabi MM, Grob D, Novotny JE, Antinnes JA: Clinical validation of functional flexion/extension radiographs of the cervical spine. Spine (Phila Pa 1976) 18:120–127, 1993
3. Ebraheim NA, Lu J, Biyani A, Brown JA, Yeasting RA:

Spine

SPINE Volume 37, Number 21, pp E1318–E1325

BIOMECHANICS

Kinematics of the Thoracic Spine in Trunk Rotation

In Vivo 3-Dimensional Analysis

Takahito Fujimori, MD, PhD,* Motoki Iwasaki, MD, PhD,* Yukitaka Nagamoto, MD, PhD,* Takahiro Ishii, MD, PhD,† Masafumi Kashii, MD, PhD,* Tsuyoshi Murase, MD, PhD,* Tsuyoshi Sugiura, MD,* Yohei Matsuo, MD,* Kazuomi Sugamoto, MD, PhD,‡ and Hideki Yoshikawa, MD, PhD*

Study Design. *In vivo* 3-dimensional (3D) study of the thoracic spine.

Objective. To demonstrate axial rotations (ARs) and coupled motions of the thoracic spine.

Summary of Background Data. *In vivo* 3D kinematics of the thoracic spine in trunk rotation with intact thorax and soft tissues has not been well-known.

There were no quantitative data of AR in the consecutive thoracic spinal segments. Patterns of coupled motion with AR have been controversial.

Methods. Thirteen healthy volunteers underwent 3D computed tomography of the thoracic spine in 3 positions; neutral, right, and left maximum trunk rotation. Relative motions of vertebrae were calculated by automatically superimposing the vertebrae in a neutral position over images in rotational positions, using voxel-based registration. Motions were represented with 6 degrees of freedom by Euler angles and translations on the local coordinate system.

Results. Mean (±SD) relative rotational angles of T1 with respect to L1 to 1 side were 24.9° ± 4.9° in maximum trunk rotation. AR of each thoracic segment with respect to the inferior adjacent vertebra to 1 side was 1.2° ± 0.8° at T1–T2, 1.6° ± 0.7° at T2–T3, 1.4° ± 0.9° at T3–T4, 1.6° ± 0.8° at T4–T5, 1.8° ± 0.7° at T5–T6, 1.9° ± 0.6° at T6–T7, 2.3° ± 0.7° at T7–T8, 2.5° ± 0.8° at T8–T9, 2.7° ± 0.6° at T9–T10, 2.6° ± 0.8° at T10–T11, 1.3° ± 0.7° at T11–T12, and 0.5° ± 0.4° at T12–L1. Significantly larger segmental AR was observed at the middle thoracic segments (T6–T11) than at the upper (T1–T6) and lower (T11–L1) segments. At the upper thoracic segments, coupled lateral bending with AR was observed in the same direction as AR. However, at the middle and lower thoracic segments, coupled lateral bending occurred both in the same and opposite directions.

Conclusion. *In vivo* 3D ARs and coupled motions of the consecutive thoracic spinal segments in trunk rotation were investigated accurately for the first time.

Key words: thoracic spine, rotation, coupling motion, *in vivo*, 3-dimensional. **Spine 2012;37:E1318–E1328**

Spinal biomechanics and kinesiology are essential for better comprehension of the pathogenesis of spinal disorders and therapies. Relationships between biomechanics and spinal disorders have been discussed in previous research.[1] Compared with other regions of the spine, the thoracic spine is unique in both anatomy and potential disorders. The disc of the thoracic spine represents a reduced amount of height in ratio to the vertebral body, and the angle of facet joints is steeper than the cervical spine and is more frontally oriented than the lumbar spine. Many spinal traumas occur in the thoracolumbar region and scoliotic deformity frequently starts in the midthoracic region. Correction of rotational deformity of scoliosis is a technically demanding procedure[2]; however, it is not well-known how much axial rotation (AR) could physiologically occur in the normal thoracic spine. The kinematics of the thoracic spine has been investigated on *in vitro* cadaveric studies[3–5] and mathematical models[6] and *in vivo* by using the 3-space track system[7–8] or invasive pin insertion method.[9–10] Although cadaver studies and mathematical models enabled accurate measurement, they might not be physiological in relation to the lack of rib cage, real muscle tone, or intra-abdominal pressure. In many cadaver studies, analysis was performed in various spinal units of limited numbers on elderly subjects. The decision of whether to simulate ideal force or torque *in vivo* motions may be difficult. The 3-space track system was a noninvasive method; however, it was difficult to assess intervertebral motions of each single spinal segment because of the potential for measurement errors.[11] Measurement by the pin insertion method was accurate and physiological; however, it seemed to be too invasive to be performed at each spinal segment. Thus, *in vivo* 3-dimensional

From the *Departments of Orthopedic Surgery; †Department of Orthopedic Surgery, Kaizuka City Hospital, Osaka, Japan; and ‡Orthopedic Biomaterial Science, Osaka University Graduate School of Medicine, Osaka, Japan.

Acknowledgment date: April 30, 2012. Revision date: June 18, 2012. Acceptance date: June 22, 2012.

The manuscript submitted does not contain information about medical devices or drugs.

This work was supported by a grant-in-aid for Scientific Research C (KAKENHI: 22591632) from the Ministry of Education, Culture, Sports, and Technology, Japan; and by an AO Spine research grant.

No benefits in any form have been or will be received from a commercial party related directly or indirectly to the subject of this manuscript.

Address correspondence and reprint requests to Takahito Fujimori, MD, PhD, Department of Orthopaedic Surgery, Osaka University Graduate School of Medicine, 2–2 Yamadaoka, Suita, Osaka 565–0871, Japan; E-mail: takahito-f@hotmail.co.jp

DOI: 10.1097/BRS.0b013e318267254b